Performances of a VIPA-based spectrometer for Brillouin scattering experiments in the diamond anvil cell under laser heating

A. Forestier, G. Weck, Frédéric Datchi, P. Loubeyre

Performances of a VIPA-based Spectrometer for Brillouin Scattering Experiments in the Diamond Anvil Cell under Laser Heating

A. Forestier[a,b,*], G. Weck[a,b,*], F. Datchi[c] and P. Loubeyre[a,b]

[a]CEA DAM DIF, F-91297 Arpajon, France
[b]Université Paris-Saclay, CEA, Laboratoire Matière en Conditions Extrêmes, 91680 Bruyères-le-Châtel, France
[c]Sorbonne Université, Muséum National d'Histoire Naturelle, UMR CNRS 7590, Institut de Minéralogie, de Physique des Matériaux et de Cosmochimie, IMPMC, 75005 Paris, France

ARTICLE HISTORY
Compiled November 25, 2022

ABSTRACT
VIPA-based Brillouin spectroscopy is implemented for *in-situ* measurements at high pressure and temperature in laser-heated diamond anvil cells. Its performances are compared to those of the widely used Tandem Fabry-Perot instrument. A significant reduction of the collection time is in particular enabled. The usefulness of VIPA-Brillouin spectroscopy for High Pressure studies is here illustrated by revisiting the nitrogen melting curve up to 45 GPa. VIPA-Brillouin spectroscopy has the potential to become an important platform to investigate the equation of state properties of warm dense molecular systems.

KEYWORDS
High pressure, Brillouin scattering, VIPA, Laser heating, Diamond anvil cell, Nitrogen, Melting

1. Introduction

Brillouin spectroscopy enables to measure by inelastic light scattering the frequency of acoustic vibrations in a sample. One can then straightforwardly deduce the adiabatic sound velocity and the elastic moduli of the sample [1]. This optical technique is well suited for high pressure experiments using diamond anvil cells (DAC), not only allowing to characterize elastic properties of crystalline and amorphous solids under extreme conditions, but also the detection of pressure-induced phase transitions in the sample through sound speed discontinuities. For example, Brillouin scattering has been used, in conjunction with x-ray diffraction, to develop a primary pressure scale using MgO, c-BN and SiC crystals [2–4], to study the anomalous elasticity in silica glass [5,6], or to identify the transition of water ice to its symmetric X form at high pressures [7]. Also, coupled to resistive or laser heating DAC techniques, Brillouin measurements can offer a microscopic diagnostic of structural transitions at high P-T. [8,9]. The pressure-temperature equation of state of hot dense fluids can be obtained through the thermodynamic integration of the measured sound velocity [10]. The sample refractive index can also be obtained from Brillouin data [11]. Interestingly, Brillouin

*A. Forestier. alforestier@gmail.com. G. Weck. gunnar.weck@cea.fr

data can be used to study mixtures at extreme pressure and temperature conditions [12]. Finally, it may help to investigate further fluid polymorphism at high density, providing complementary information to x-ray diffraction data. Thereof, applications range from geophysics and planetary interiors research, to materials characterization and fundamental physics.

The major challenges for Brillouin measurements lies in the weak intensity of the scattered light with respect to the laser excitation (its intensity is of the order of $\sim 10^5$ times smaller than the elastic scattering one), and the extremely small spectral shift to be detected, *i.e.* $\Delta\nu$ is in the $1 - 200$ GHz range, corresponding to $0.03 - 7$ cm^{-1}. A Brillouin frequencies analyzer must thus provide high spectral resolving power and very high contrast. The Tandem Fabry-Perot (TFP) interferometer developed by J. R. Sandercock in the 1980s [13] fulfills these requirements and it has been most exclusively used in high pressure research over the past four decades. The TFP is based on the synchronized scanning of two Fabry-Perot etalons allowing to temporally disperse the Brillouin spectrum with sufficient contrast. Because of the very small sample volumes which are accessible in the DAC, the time needed to obtain a good signal-to-background ratio with the TFP is typically of the order of minutes to hours, depending on the pressure range investigated and the sample Brillouin efficiency. This can make such Brillouin measurements in the *in-situ* laser heating DAC quite challenging, since it can be very difficult to maintain a stable sample temperature over several minutes due to fluctuations in the laser absorption and/or sometimes to chemical reactions of the hot sample with its surrounding materials. Hence there is a need for higher Brillouin signal throughput to be able to measure the sound velocities of warm dense molecular systems.

Recently, the VIPA (*Virtually Imaged Phased Array*) technology has allowed to measure Brillouin spectra without the need of frequency scan, by implementing spatial dispersion so that the full spectrum can be simultaneously recorded using a bi-dimensional pixel array [14–17]. It was shown on standard samples that this approach enables to increase signal throughput by several orders of magnitude with respect to the TFP [18,19]. Up to now, VIPA-based instruments have been mainly used for Brillouin measurements on biological systems under ambient conditions. To our knowledge, it has never been implemented in the field of high pressure research.

We here below demonstrate the feasibility of the VIPA based Brillouin spectroscopy measurements for high pressure samples in laser-heating DACs and we discuss the advantages and drawbacks of that approach compared to using the TFP device. Some details for implementing the VIPA instrument on a high pressure bench are also given. Brillouin measurements on pressurized nitrogen around its melting line up to 45 GPa and 2000 K are presented as a qualifying test.

2. Experimental set-up

To perform the comparative present study, the VIPA-based spectrometer was added to an existing high pressure-high temperature Brillouin bench, constructed around a TFP interferometer and a CO_2 laser heating of the DAC. The temperature was estimated from the sample thermal emission collected over 550-950 nm. The Brillouin shift depends on the chosen scattering geometry. Here, Brillouin measurements were performed in both the back-scattering and platelet geometries and so the measured Brillouin shift $\Delta\nu$ is related to the sample sound velocity V_S and refractive index n,

respectively by:

$$\Delta\nu = \frac{2nV_S}{\lambda} \tag{1}$$

and

$$\Delta\nu = (2V_S/\lambda)\sin(\theta/2), \tag{2}$$

where λ is the excitation laser wavelength and θ is the scattering angle (angle between the incident and scattered light wavevectors, in forward arrangement with a symmetric finite angle with respect to the sample normal) [1]. The platelet geometry allows to get rid of the sample refractive index thanks to the Snell-Descartes refraction inside the sample. In platelet geometry, both longitudinal and transverse modes are probed while in back-scattering geometry, only longitudinal acoustic vibrations can be detected due to selection rules [13].

Figure 1 shows a sketch of the optical set-up. Different laser excitation wavelengths have been used in the two Brillouin spectroscopies: 514 nm for measurements using the TFP (TFP-1 model, JRS Optical Instruments) and 457 nm using the VIPA-based spectrometer (Brillouin hyperfine spectrometer, Light Machinery Inc.). Our VIPA hyperfine spectrometer was designed to operate with a 457 nm excitation wavelength. That excitation wavelength was selected to limit the background contribution on the Brillouin spectra coming from the thermal self-emission of the sample at high temperature. On the other hand, at the time of present experiments, the TFP-1 interferometer was equipped with mirrors operating in the range 490-540 nm. The comparison of the two instruments was thus performed using different excitation wavelengths. The 514 nm radiation is produced by a single mode Coherent Genesis CX laser and the 457 nm one by a single mode Cobolt 05-01 Twist laser. The excitation wavelength is changed using two flip-mirrors (FM1 and FM2 in figure 1), such as both lasers follow a common optical path except for the final collection of scattered light into the TFP interferometer or the VIPA hyperfine spectrometer. The optical design allows also to switch from back-scattering to platelet scattering geometry by taking advantage of the polarization of light. By setting the angle of the first half-wave plate, the polarizing beam splitter cube PBS1 reflects the laser towards excitation path labeled 1 in figure 1 for back-scattering geometry, or transmits light towards path labeled 2 for measurements in platelet geometry with 30° incidence (60° scattering angle). The excitation laser is converted to circular polarization by a quarter-wave plate before its focusing in the DAC cavity. By converting the scattered light back to linear polarization, it is fully reflected on PBS2. Achromats or long working distance microscope objectives can be used as focusing optics on the sample (path 1 and 2) depending on the space requirements around the DAC.

The scattered light is focused on the TFP-1 input pinhole of 150 µm diameter by a 75 mm achromat. Coupled with a $f = 60$ mm achromat for signal collection (path 1), it leads to a ~ 120 µm in diameter region at the sample. A higher confocality can be reached by using a long working distance 10x objective as collection optics, leading to a ~ 40 µm spot diameter at the sample.

In the VIPA hyperfine spectrometer configuration, the signal is coupled into a single-mode (SM) optical fiber of ~ 3.5 µm core field diameter using a 40 mm focal length collimator and that requires a very stringent alignment. The collection SM fiber delivers the collected signal to one or two serialized Pump Killer modules (Light Machinery

Inc.) dedicated to the filtering of elastic scattering light (details will be given below) prior to the coupling into the VIPA hyperfine spectrometer using another SM fiber. The use of such single mode fiber leads to very sharp spatial filtering: by using a $f = 60$ mm achromat in path 1, the collection spot diameter at the sample is approximately 5 µm. The use of a 10x objective leads to a collection spot diameter of the order of 2 µm. The use of a beam expander, positioned in-between the 457 nm laser and the focusing optics, reduces the excitation spot at the sample to approximately the same size as the signal collection area.

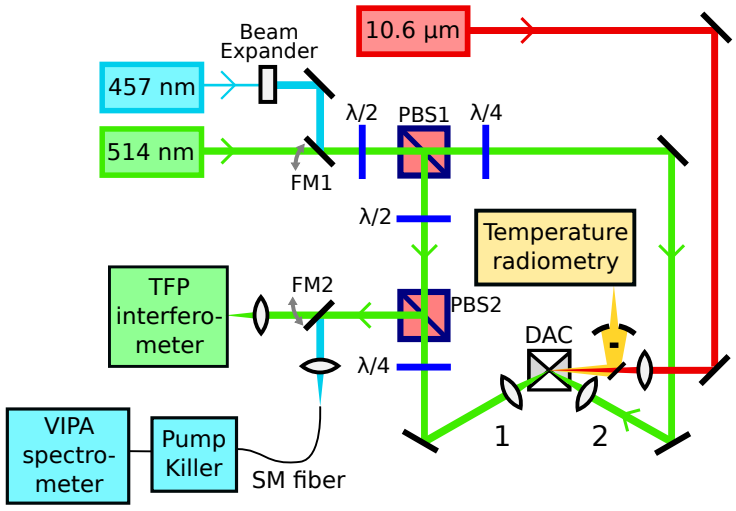

Figure 1. Sketch of the experimental set-up used during this work. Flip-mirrors FM1 and FM2 are used to switch from the TFP-1 configuration (514 nm, green path) to the VIPA hyperfine spectrometer configuration (457 nm, blue path). The half-wave plate before the polarizing beam-splitter PBS1 allow to switch from backscattering to platelet geometry (see text). The sample is excited by the laser beam through optical path 1 for backscattering geometry or through path 2 for platelet geometry. The scattered light is collected through path 1 and forwarded to the TFP-1 or to the VIPA hyperfine spectrometer. The 10.6 µm CO_2 laser radiation is focused in the DAC cavity for laser heating of the sample (red path). Thermal radiation emitted from the sample is collected by a Schwarzschild objective and analyzed into the spectrometer dedicated to temperature radiometry (yellow path).

To perform laser heating of the sample, a 10.6 µm CO_2 laser radiation (Synrad firestar f201, 200 W power) is focused by a $f = 75$ mm ZnSe lens in the DAC sample chamber with a $\sim 25°$ elevation angle. The thermal emission from the sample is collected by a finite conjugate Schwarzschild objective preventing any chromatic aberrations (yellow path in figure 1). It is then coupled into the spectrometer (Andor Technology) dedicated to the temperature radiometry. The temperature of the sample is estimated by fitting the spectrum with the Planck formula assuming a wavelength-independant grey-body thermal emission. The temperature uncertainty is estimated by the sliding two-color pyrometry analysis, as described in details in Ref. [20].

3. Tandem Fabry-Perot vs. VIPA Brillouin spectroscopy

Up to now, the most convenient instrument to use for Brillouin spectroscopy was based on Fabry-Perot interferometry. In the TFP-1 device, the Brillouin scattered light from the sample undergoes 3+3 passes (six in total) through two tunable Fabry-Perot (FP) etalons, before reaching a photon counter (Hamamatsu C11202) as shown in figure 2(a). Each FP only transmits wavelengths λ satisfying the relation $e = p\lambda/2$ where

e is the FP spacing and p an integer. Successive interference orders are separated by the free spectral range FSR related to e through FSR $= c/(2e)$, where c is the speed of light. The two FP interferometers are slightly detuned so that only one interference order is selected. Therefore, by scanning synchronously the spacings of the two FP the spectrum can be collected over a time interval and retrieved through a multichannel analyser. Synchronicity is maintained by design since both FP are scanned through a common piezo-electrically driven translation stage as sketched in figure 2(a), top panel. Figure 2(a), bottom panel shows a typical Brillouin spectrum obtained on a fluid H_2O sample loaded in the DAC at $\sim$ 1 GPa in platelet geometry. The TFP-1 instrument has the advantage to provide tunable FSR, resolution, and spectral range up to 1 THz. The 3+3 passes through the FP etalons lead to a very high contrast of $\sim 10^{10}$. Recent optimizations of the instrument have been shown to provide a $\sim 10^{15}$ contrast [21]. The main drawback of using the TFP-1 device for measurements under extreme conditions is the scanning time needed to reach the desired signal-to-noise ratio of the spectrum.

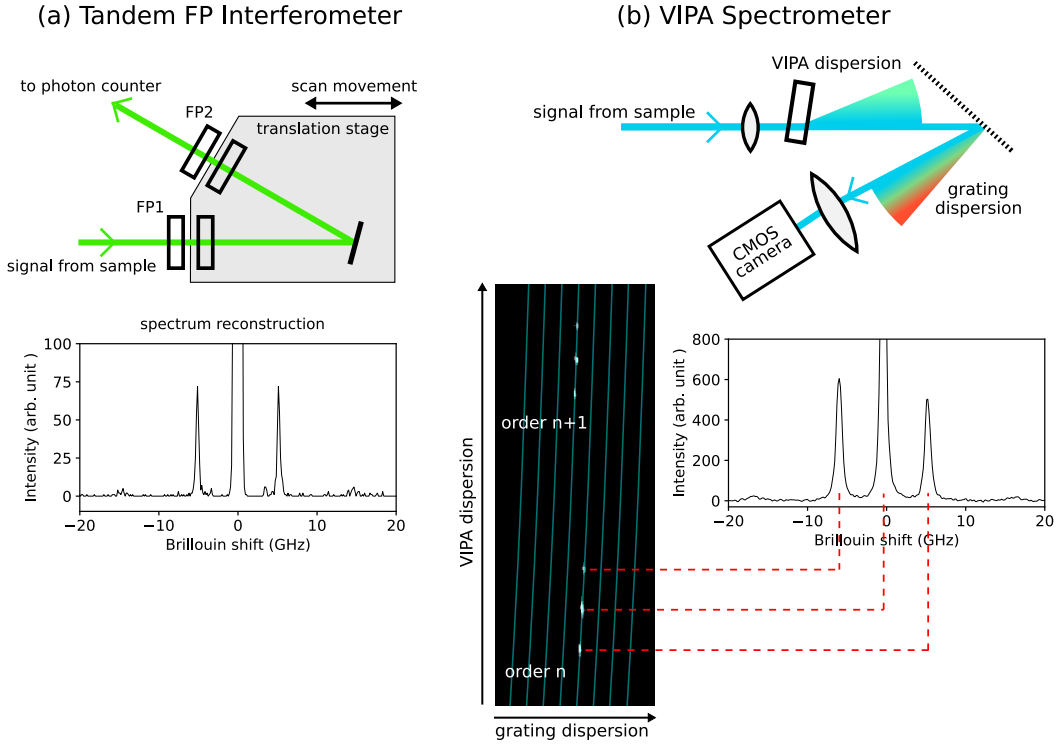

Figure 2. Principle of Brillouin spectroscopy using (a) the 3+3 pass Tandem Fabry-Perot interferometer or (b) the VIPA hyperfine spectrometer. In the TFP-1 (a), the scattered light undergoes three passes through two tunable Fabry-Perot etalons (only one pass is represented for simplicity). The spectrum is so decomposed in time by scanning the translation stage, and sequentially reconstructed. In the VIPA hyperfine spectrometer (b), the spectrum is dispersed by the VIPA etalon in the vertical direction, then by the diffraction grating in the horizontal direction and finally projected on a camera by a lens. The obtained image allows reconstruction of the Brillouin spectrum after calibration: the image is integrated along the blue stripes taking into account equivalent features from the successive VIPA interference orders.

The VIPA hyperfine spectrometer implements a *spatial* dispersion of the scattered light to be analyzed. The VIPA itself is a SiO_2 etalon of fixed thickness in which a strong angular dispersion is produced. It has a narrow entrance window in a virtually 100% reflective surface, while the output surface is only partially reflective. The light is focused through the entrance window by the mean of a cylindrical lens, such as multiple

interferences in the VIPA etalon lead to collimated output light with propagation angle depending on the wavelength [22]. The VIPA provides high spectral dispersion but with a fixed FSR (in our case 38 GHz). In the hyperfine spectrometer, the light exiting the VIPA is then dispersed by a 79 grooves/mm diffraction grating in the perpendicular direction as shown in figure 2(b), top panel. The dispersed light is finally focused on a CMOS camera (Hamamatsu ORCA-Fusion C14440-20UP). The spectral features are resolved from their position on the two-dimensional image. The diffraction grating stage allows to unambiguously discern signals separated by integer multiples of the VIPA FSR, that would otherwise overlap.

The image output obtained in platelet geometry from a fluid H_2O sample loaded in the DAC at ~ 1 GPa is shown in figure 2(b), bottom panel. Two interference orders from the VIPA are shown. For each, the Rayleigh line as well as both Stokes and anti-Stokes peaks from the sample are visible. The Brillouin spectrum is retrieved by "unwrapping" the image along the blue stripes, as shown in figure 2(b), bottom panel. The calibration lines are obtained by adjusting a physical model of the instrument dispersion (based on a paraxial solution [23]) on both the 457 nm laser radiation and on a broadband spectrum produced by a light-emitting diode. Calibration stripes are separated by exactly one VIPA FSR in the grating dispersion direction. Since redundant information is present in a single image, successive interference orders from the VIPA are averaged in the spectrum. The VIPA hyperfine spectrometer has a fixed FSR and resolution (38 GHz and 0.8 GHz in our case, respectively). The contrast provided by the VIPA alone (approximately 10^5) is often insufficient for proper measurements. Thus, additional filtering of the elastic signal is often required, as described below.

The main advantage of the Brillouin VIPA spectroscopy lies in the fact that the spectrum is decomposed *in space* such that the entire spectrum is simultaneously obtained on the camera sensor. That can considerably decrease the accumulation time needed to obtain a given Brillouin signal-to-noise ratio compared to the use of the TFP-1 instrument. Many factors though can affect the signal throughput of a given technique and so the VIPA hyperfine spectrometer performances for Brillouin spectroscopy under extreme conditions are specifically examined here below.

4. Elastic scattering suppression

Several strategies have been used to reach higher contrast using VIPA-based instruments, for example by using two VIPA etalons in crossed configuration [16,17], or by reducing the elastic signal beforehand, *e.g.* using a vapour absorption cell [19] or by destructive interference [24]. In our case, the hyperfine Brillouin spectrometer can be associated with one or two additional filtering module(s) [called Pump Killer module(s)], inserted prior to the spectrometer stage to strongly attenuate the elastic scattering by destructive interference. Such module has fibered input and output, and is based on a properly tuned FP etalon upon which the scattered light reflects twice leading to strong attenuation of the laser line at the output. Each additional PK module increases the contrast by more than 10^3. The FSR of our PK etalons are fixed at 76 GHz (i.e, twice the VIPA FSR), with the drawback that the spectrometer is blind to any signal with integer multiples of 76 GHz frequency. The performances using one or two successive Pump Killer (PK) modules are illustrated with the Brillouin spectra in backscattering geometry from a fluid H_2O sample at ~ 1 GPa, as shown in figure 3. The corresponding raw images on the CMOS camera are shown as insets in figure 3. In both spectra, the central Rayleigh line is visible as well as the Stokes and

anti-Stokes peaks of the sample at 14.46 GHz (red arrows in figure 3). Narrow, intense peaks located at every 38 GHz integer multiples (the VIPA FSR) are observed in the spectrum obtained with one PK, while they are completely absent when two PK are used. A weaker peak is observed in both spectra at 188.06 GHz, which is ascribed to the Brillouin signal of the diamond anvils (blue arrows in figure 3). One can note a slight intensity asymmetry between Stokes and anti-Stokes peaks, which is mainly due to a small detuning of the PK modules.

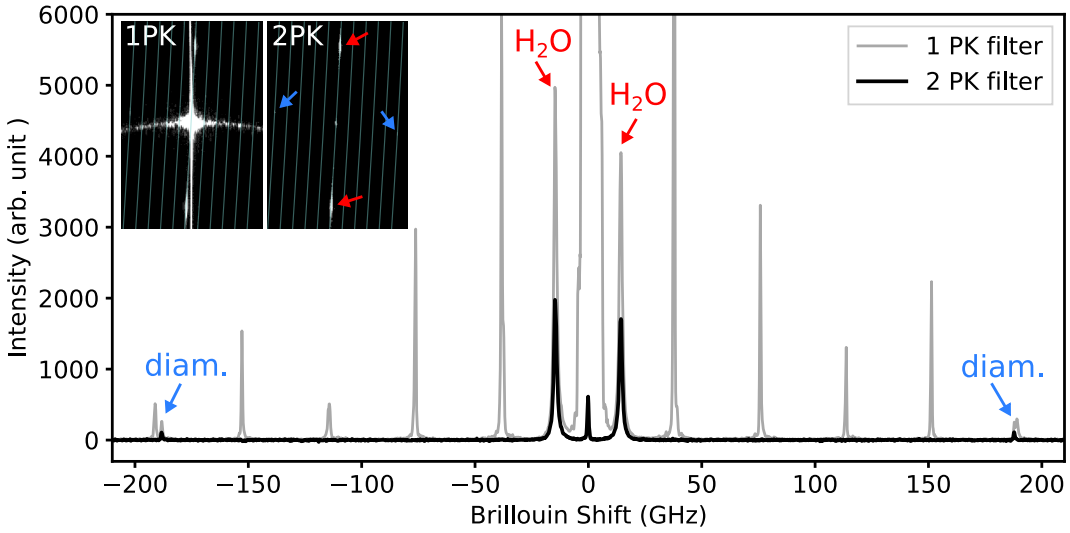

Figure 3. Brillouin spectra of a fluid H_2O sample near 1 GPa obtained in backscattering geometry. One, or two successive Pump Killer modules were inserted for elastic scattering attenuation (grey and black spectrum, respectively). The inset shows the corresponding raw images on the CMOS camera (only one VIPA interference order region is shown). Red arrows indicate the H_2O signals, and blue arrows the signal from diamond anvils. The laser power on the sample was set to $\sim$ 90 mW, and was focused through a long distance x20 Mitutoyo Plan Apo SL objective (NA = 0.28). In this particular case a $f = 11$ mm aspheric lens was used for coupling in the SM fiber. The acquisition time was set to 3×5 s.

As expected, the central Rayleigh line intensity is strongly reduced when using two Pump Killer modules. However, the signal intensity from the sample is also approximately twice weaker. This is due to losses in the additional PK module, mainly from the insertion in the output SM fiber. Note that the absolute intensity of the Rayleigh line in a given spectrum strongly depends on the focusing in the sample, on the NA of the objective or on lens used, and on the incidence angle of the excitation laser into the DAC, since it mainly originates from the reflected light at the diamond-air and diamond-sample interfaces.

On the camera sensor image obtained using only one PK (inset in figure 3), the central elastic line strongly dribbles in both directions of dispersion (as far as $\sim$ 8 GHz in fig. 3) preventing proper measurements in this low frequency shift region. That signal produces artifacts in the unwrapping process at every intersections of the Rayleigh line with the calibrated "unwrapping" lines (blue stripes in insets of fig. 3). These cross-talk artifacts lead to the observed set of peaks at every $p \times$ FSR in the corresponding spectrum. When two PK are used, the Rayleigh line is sufficiently attenuated to completely suppress the cross-talk. In short, one may choose using one or two PK modules depending on (i) the intensity of the Rayleigh line , (ii) the relative intensity of the Brillouin signal, (iii) the frequency range of the sample Brillouin peaks, and their possible spectral overlap with cross-talk artifacts at every $p \times$ FSR.

5. Quantitative assessments

In order to assess the performances of the VIPA hyperfine spectrometer more quantitatively, we compare below the data obtained with the VIPA instrument to those with the TFP-1 interferometer on identical samples. A protocol similar to the one of references 18 and 19 was followed. For various acquisition times –or number of scans with the TFP-1–, series of ten spectra were recorded on a fluid H_2O sample at ~ 1 GPa. Both back-scattering and platelet geometries were measured, and only one PK module was inserted. For each spectrum, the sample Brillouin Stokes and anti-Stokes peaks were fitted using a lorentzian profile:

$$I(\nu) = \frac{I_0}{1 + \left(\frac{\nu - \nu_0}{\Gamma/2}\right)^2} \tag{3}$$

where I_0 is the height of the peak, ν_0 its spectral position and Γ its full width at half maximum (FWHM). Typical Brillouin spectra obtained in back-scattering geometry with both instruments are shown in figure 4, along with the fitted lineshapes plotted in red. The different spectral positions of the Brillouin peaks obtained with the VIPA hyperfine and the TFP-1 spectrometers arises from the different laser excitation wavelengths used for each measurements and is quantified by the $1/\lambda$ dependence of the Brillouin shift. Such series of measurement allowed to quantify the reproducibility of the measured spectral position and FWHM as a function of the acquisition time. To do so, we calculated the standard deviation of the spectral position and width over the ten spectra series for each acquisition duration (the average positions and widths from Stokes and anti-Stokes peaks were used). We also calculated the signal-to-noise ratio (SNR) by taking the mean peak height $\langle I_0 \rangle$ divided by the standard deviation of the background noise σ_{noise}, the latter being evaluated in a region where no spectral features are present, as shown in blue in the insets of figure 4. The following formula was used:

$$\text{SNR} = 20\log_{10}\left(\langle I_0 \rangle / \sigma_{\text{noise}}\right) \tag{4}$$

.

The obtained standard deviations and the SNR as a function of acquisition time are presented in figure 5. The number of TFP-1 scans was converted into acquisition duration using the measured value of 640 ms/scan, accounting not only for the time spent on each TFP-1 channel but also for operating time between each channel. The power on the sample was set close to ~ 100 mW for both excitation lasers. In fact, results plotted in figure 5 are corrected for the small laser power variations, and for the $1/\lambda^4$ factor in the scattering intensities since the two Brillouin spectroscopy data-sets were measured with different excitation laser wavelengths.

Looking at figure 5 (a,b) and (d,e), for increasing acquisition time, one can observe a strong decrease in the standard deviation on peak position and on FWHM. For both instruments, the precision in positions and in FWHM tends toward ~ 5 MHz and ~ 20 MHz, respectively, in good agreement with previous reports [18,19]. However, for reaching a given precision, the VIPA hyperfine spectrometer is more than ten times faster than the TFP-1 interferometer. That is also true for a given SNR value, as shown in figure 5(c) and (f),

In general, the signal noise arises from multiple contributions [25]. The main ones are

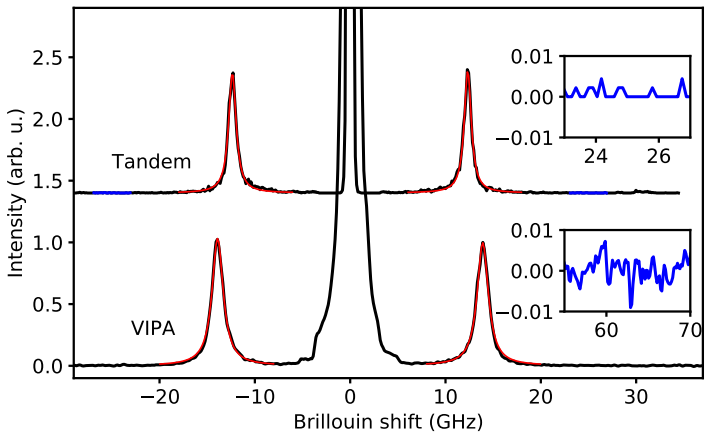

Figure 4. Typical Brillouin spectra obtained with the TFP-1 interferometer (top spectrum) and the VIPA hyperfine spectrometer (bottom spectrum) for a H_2O sample at $\sim$ 1 GPa. Spectra were measured in back-scattering geometry. The acquisition time was set to 1 s with the VIPA hyperfine spectrometer and to 19.2 s with the TFP-1 (30 scans), leading to a similar signal-to-noise ratio. The fitted lorentzian functions are shown in red. Both insets correspond to the background regions where the noise was sampled for SNR estimation.

(i) the photon shot noise in the signal, proportional to the signal intensity itself (thus $\propto \sqrt{t}$ with t the acquisition time), (ii) the dark shot noise from thermally excited electrons in the optical sensor (also varying as $\propto \sqrt{t}$), and (iii) the readout noise generated at signal amplification and digitization (independent of t). In our calculated SNR value, the photon shot noise is not included since only the background noise is considered and since it is intrinsically identical for both instruments.

Looking at figure 5(c) and (f), the SNR obtained with the VIPA hyperfine spectrometer in the short integration time regime shows an increasing trend with a steeper slope than the 0.5 slope expected for a $\sqrt{t}$ law in log scale. We rather found values close to 0.9 for both platelet and back-scattering measurements [see figure 5(c) and (f)]. This implies that the SNR is limited by the readout noise of the CMOS camera rather than by the camera dark current in this short integration time range. For longer integration times, the linear SNR increase is almost following the expected 0.5 slope in the dark shot noise limited regime (we find values in-between 0.5 and 0.6). On the other hand, a slope close to 0.5 is found for the TFP-1 measurements (0.45 and 0.47 for platelet and backscattering geometries, respectively) over the whole acquisition duration range and for both scattering geometries, showing that the readout noise is negligible in that case. This difference has important implications because the CMOS camera used in the VIPA hyperfine spectrometer is limited to a maximum of 10 s single acquisition time. Summing successive acquisitions in the dark noise limited regime is equivalent to performing a longer single acquisition. Whereas, in the short acquisition regime, readout noise adds up and so summing successive spectra does not improve the SNR or hardly. If the signal from a given sample is too weak to really emerge from the readout noise even for the longest possible acquisition time, its visibility will not be improved by summing multiple spectra. This is an important drawback with respect to the TFP-1 system for which virtually any signal can be extracted from noise by increasing the measurement time.

Typical Brillouin anti-Stokes peaks measured either with the TFP-1 (red dashed curve) or the VIPA hyperfine spectrometers (black solid line) under identical conditions are compared in Figure 6 for the longest investigated acquisition time for each instrument.

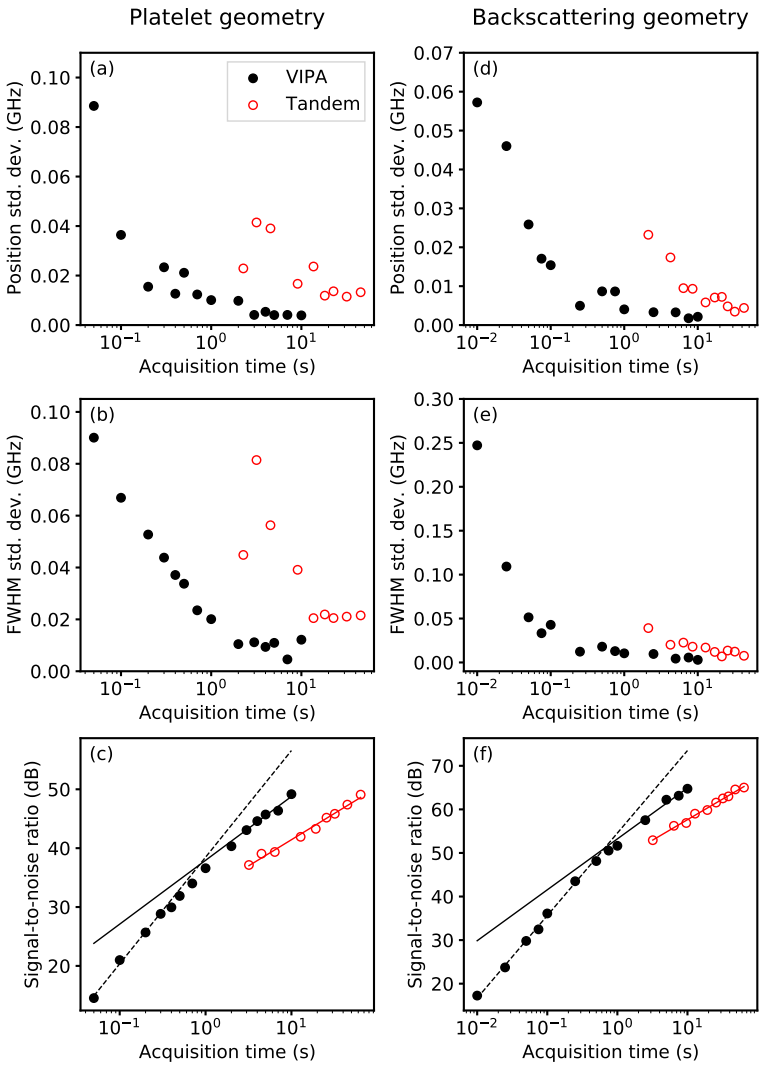

Figure 5. Standard deviation for the spectral position and FWHM of the measured Brillouin peaks (a,b and d,e), and SNR (c, f) as function of acquisition time. Data were obtained in a fluid H_2O sample near 1 GPa using the TFP-1 interferometer (red, open symbols) and the VIPA hyperfine spectrometer (black symbols). The left panel corresponds to platelet scattering geometry (a,b and c) and the right panel to back-scattering geometry (d,e and f). In the platelet scattering geometry case, two Optosigma M Plan Apo PAL 5x objectives (NA = 0.14) were used for excitation and collection optical paths. For back-scattering geometry, the incidence angle on the DAC was reduced so that a larger NA objective could be used (a Mitutoyo Plan Apo 10x, NA = 0.28). Only one PK module was inserted before the VIPA hyperfine spectrometer. In (c) and (f), red lines correspond to linear fits on the SNR measured with the TFP-1 interferometer. Linear fits on the SNR measured with the VIPA hyperfine spectrometer in the short and long acquisition time regimes are shown as black dashed and solid lines, respectively.

The Brillouin peak FWHM depends on the viscosity of the sample, on the numerical aperture of the collection optics (which determines the range of measured scattering wavevector directions) and on the scattering geometry, but not on the excitation wavelength [18]. However, it is clear in figure 6 that the peaks obtained with the VIPA hyperfine spectrometer are significantly broadened compared to those with the TFP-1 system. The TFP-1 has a narrower response function which enables to measure FWHM values close to the intrinsic Brillouin linewidths. Indeed, FWHM values obtained for platelet and backscattering data using the TFP-1 differ by approximately

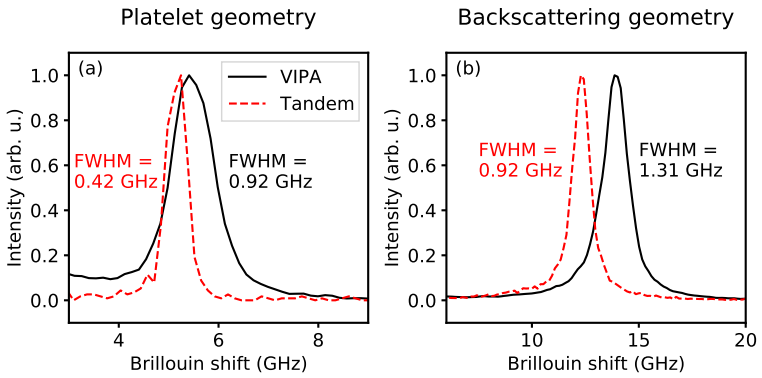

Figure 6. Brillouin anti-Stokes peak from a fluid H_2O sample loaded in the DAC at 1 GPa. Data were obtained in (a) platelet and (b) back-scattering geometry using the TFP-1 (red dashed lines) and the VIPA hyperfine spectrometer (black solid lines) with the 514 nm and 457 nm laser excitation respectively. The difference in peak position is due to the different laser wavelength used. Peaks FWHM obtained by pure lorentzian fitting are indicated in each cases. The acquisition time was set to 10 s using the VIPA hyperfine spectrometer and 64 s using the TFP-1 interferometer (100 scans).

$\sin 30°$ (within 10%), a factor expected from the different scattering geometries. By considering the FWHM obtained with the TFP-1 as intrinsic values from the sample, we evaluated a Gaussian response function for the VIPA hyperfine spectrometer of ~ 0.7 GHz FWHM. This value is in good agreement with the measured FWHM from the single-mode laser wavelength, 0.8 GHz.

In brief, the VIPA hyperfine Brillouin spectrometer allows to perform Brillouin measurements more than ten times faster than with the TFP-1 to reach equivalent precision. Furthermore, these performances are achieved in conjunction with excellent spatial filtering. The high signal throughput advantage comes at the cost of a lower spectral resolution, leading to broadening of the Brillouin peaks. The precision on the Brillouin shift stays unaffected. In platelet geometry, for a precise determination of the sound velocities from the measured Brillouin shift, the scattering angle must be precisely known. That is achieved using a calibrant having a well-known sound velocity, such as fused silica here. Doing so, the accuracy of the VIPA measurements is illustrated by the determination of the sound velocity of fluid H_2O in equilibrium with ice VI at $P = 0.98$ GPa. A shift of 5.84 GHz was measured, leading to a sound velocity of 2723 m/s using our calibrated value of the scattering angle (58.7°). This value is in excellent agreement with previous Brillouin measurements [26–31].

The spectral broadening using the VIPA hyperfine spectrometer could be a limiting factor in some cases, *e.g.* for viscosity measurements, or when two Brillouin peaks are so close in frequency that their deconvolution is no longer possible. Note also that despite the higher signal-to-noise ratio with the VIPA hyperfine set-up, extremely weak signals may be difficult to detect due to the limited integration time of the CMOS camera.

We should underline that several modifications could bring even higher signal throughput: while the use of SM fibers offers excellent spatial filtering, it also causes insertion losses at PK modules and spectrometer connections. Authors have compared performances of VIPA-based custom set-ups using single-mode or multi-mode fibers versus open-space configuration, showing that the use of multi-mode fibers lead to poor coupling into the VIPA etalon, while open-space coupling with pinhole filtering could increase signal throughput [32]. The use of open-space configuration could therefore push signal throughput even higher, but with an increased difficulty in aligning

the global set-up. Also, light focusing through diamond anvils generally leads to important spherical aberrations, all the more so as the optical aperture is large. When light is focused in the DAC with non-normal incidence (such as in platelet geometry or simply to limit the back-reflection of the laser), it also leads to strong astigmatism. Therefore, wavefront corrections of these undesirable effects could strongly increase the throughput, especially for SM fiber coupling for which the coupling efficiency is governed by the overlap of the input spot and the pure SM fiber Gaussian mode.

6. Test-case measurements on warm dense nitrogen.

In order to illustrate the usefulness of the VIPA-based spectroscopy for high pressure studies, we have performed a series of Brillouin measurements on nitrogen under high pressure and temperature. The nitrogen phase diagram has been largely investigated under pressure in the past 20 years, unraveling a rich polymorphism including several molecular solid phases, amorphous states and polymeric crystals [33–39]. The N_2 melting curve has been extensively studied theoretically [40,41] and experimentally using optical methods [42], Raman spectroscopy [34,37], or x-ray diffraction [43]. While discrepancies exist in the reported melting curves beyond $\sim$ 50 GPa, data measured below 50 GPa are in good agreement, within a 150 K uncertainty, except for ref. 42. Here, we have revisited the determination of the N_2 melting curve using Brillouin measurements in laser heated DACs.

The high pressure runs were performed on two different samples, as shown in figure 7(a), and (b). Since nitrogen cannot be directly heated by the CO_2 laser radiation, a boron-doped diamond absorber was loaded in the DAC in order to indirectly heat the N_2 sample by conduction and convection. It was laser-machined into an elliptic shape with a central hole filled with nitrogen from which the Brillouin measurement are performed [see Figures 7(a) and 7(b)]. The asymmetric, oval design is used in order to match the elliptic laser spot shape due non-normal incidence on the diamond anvil. Its external dimensions are approximately 45×35 µm and the central hole dimensions are 20 and 8 µm (major and minor axis diameters, respectively). The thickness is $\sim$ 12 µm. Figure 7(c) shows a micro-photograph of the coupler glowing at high temperature during run 1. For this run, a pit of 6.6 µm depth was machined by focused ion beam in one of the two diamond anvils, in which the C:B coupler was sitting [see fig. 7(a)] for improved stability during laser heating. The coupler is thermally insulated from the underlying diamond anvil by small KBr pieces previously installed inside the pit. In run 2, a different strategy was used: the C:B coupler sits on two KBr pads of $\sim$ 1 µm thickness for thermal insulation from the underlying diamond anvil. A very small amount of UV-curing glue on the sides of the absorber holds the latter in place during ramp heating runs. Anvils with 300 µm culets were used in both runs, and the luminescence from ruby chips loaded with the sample was used for pressure measurements [44].

Temperature was measured by optical radiometry using the C:B coupler thermal emission, assuming that the temperature of nitrogen inside the absorber hole is identical within experimental errors. The measured emission spectrum is very close to that of a perfect grey-body, as seen in figure 7(e), hence allowing a temperature determination within $100 - 150$ K uncertainty. Radial thermal gradients are small, however, axial thermal gradients remain in this sample geometry. The latter could be reduced using a capsule geometry employing two opposite couplers, as described in recent x-ray diffraction experiments [43]. Unfortunately, the optical opacity of the absorber

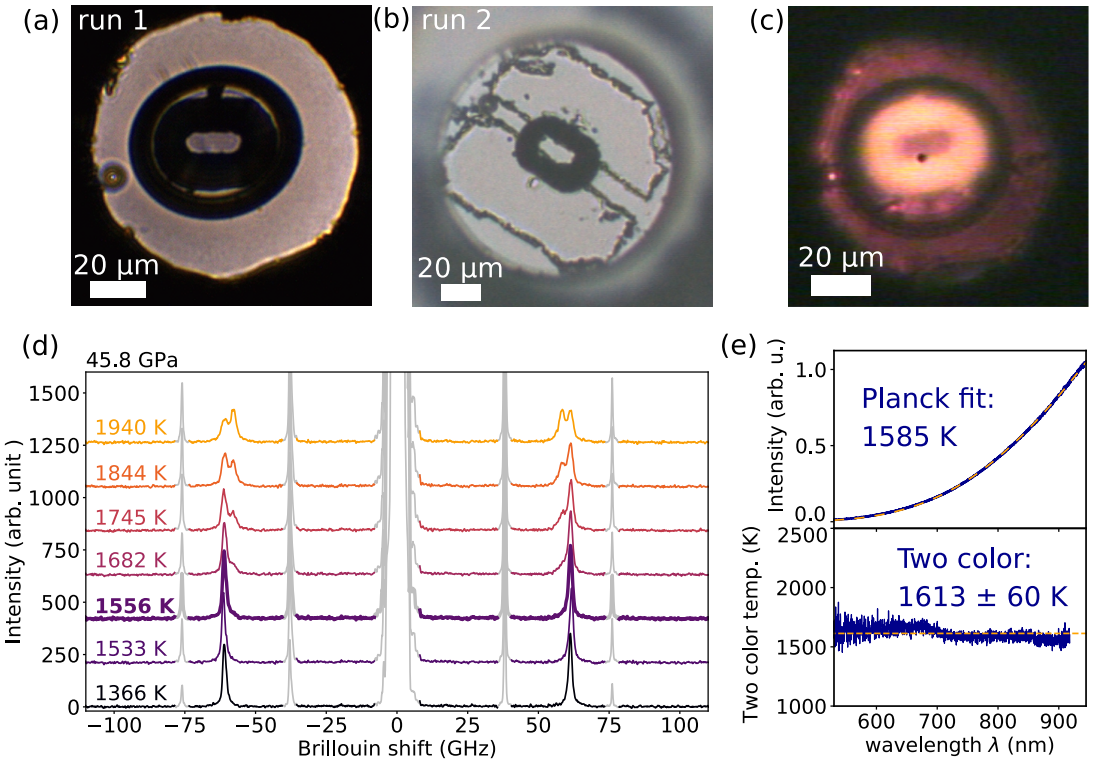

Figure 7. (a,b) Micro-photographs of the two nitrogen samples studied at high pressure (runs 1 and 2). In (a), the C:B absorber is maintained inside the elliptic pit drilled in the diamond anvil by focused ion beam. In the sample assembly of run 2 (b), the C:B absorber is positioned on ~ 1 µm-thick KBr pads for thermal insulation. (c) Micro-photograph of the "run 1" sample at high temperature showing the C:B disk homogeneously glowing. (d) Brillouin spectra of the nitrogen sample at 45.8 GPa and various temperatures, obtained in the back-scattering geometry. Spectral regions corresponding to the Rayleigh line and FSR-crosstalks are grayed out. The spectrum associated to melting is highlighted in bold. (e) An example of the temperature determination through Planck fitting and two-color pyrometry of the thermal radiation emitted by the C:B heater, corresponding to temperature value of 1585 ± 60 K, close to the melting temperature observed (d).

is presently incompatible with spectroscopic measurements in the visible. Brillouin measurements were performed in back-scattering geometry.

The 457 nm laser power was set to approximately 100 mW on the sample, and the Brillouin spectra acquisition time was 3×10 s. Note that only one PK filter was used leading to the presence of FSR-crosstalks on Brillouin spectra at integer multiples of 38 GHz, as explained above.

Typical Brillouin spectra obtained along a heating ramp at 45.8 GPa are plotted in figure 7(d). A good SNR could be obtained with only a 30 s total integration time. Below 1556 K, the spectra present a single Brillouin peak, clearly visible near 62 GHz, associated to solid nitrogen. At higher temperature, a second Brillouin peak appears downshifted by about 3 GHz with respect to the solid N_2 peak, which is ascribed to fluid nitrogen. The intensity of this peak increases with increasing temperature because the fluid volume increases within the hot spot. Even at the highest temperature reached (1940 K), the solid N_2 peak is still observed, meaning that the axial temperature gradient is still larger than the difference between the measured temperature of the absorber and the melting temperature of N_2.

Axial thermal gradients are observed since thermal insulation from the diamond anvil is made only on the absorber side. The Brillouin spectra is thus convoluting the

signal stemming from the various layers along the axial temperature gradient. This behavior is typical of laser heating experiments and is largely documented in literature [20,45]. The melting temperature was thus determined as the lowest one where the Brillouin peak of fluid N_2 was detected [shown in bold in fig. 7(d)] corresponding to 1556 K at 45.8 GPa.

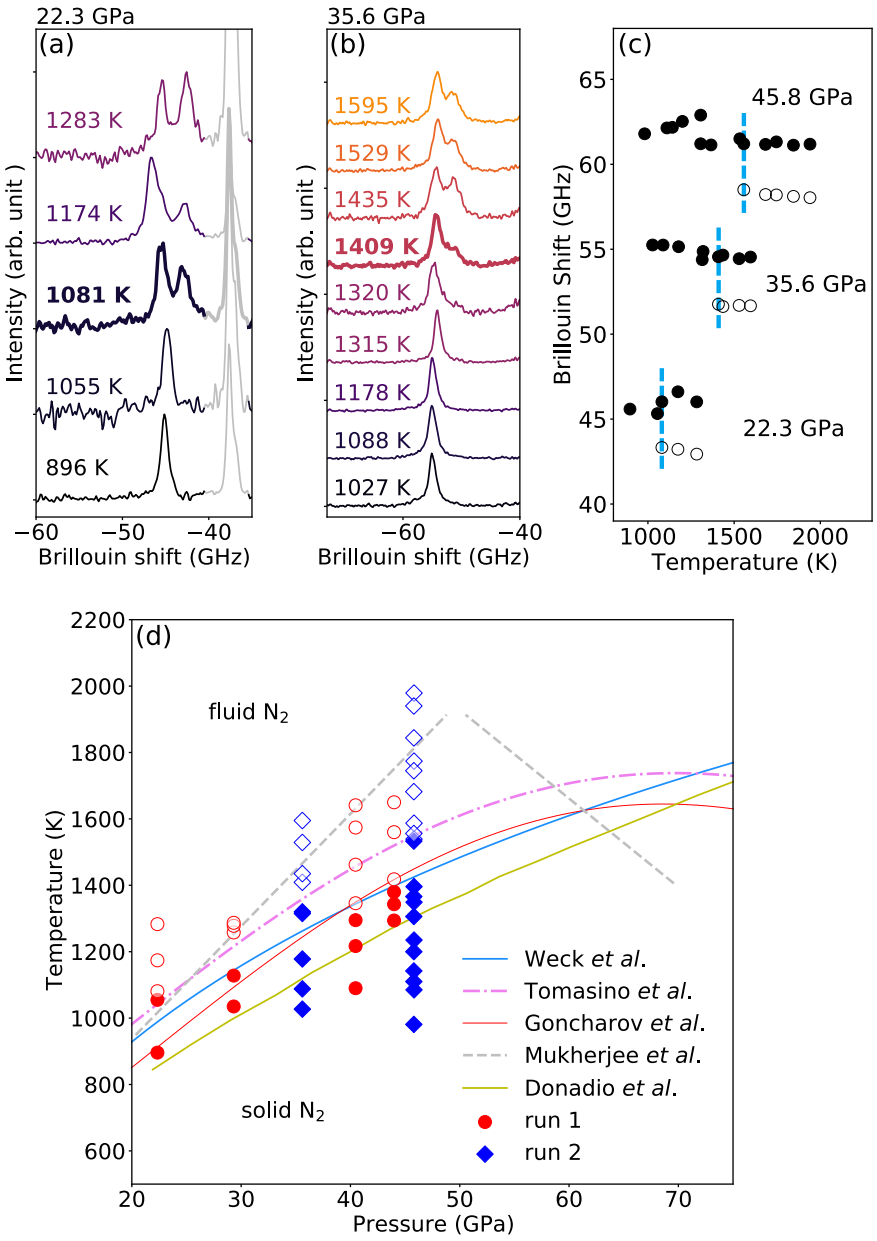

Figure 8. (a-b) Brillouin spectra (zoom on the Stokes region) of the nitrogen sample along two heating ramps at 22.3 GPa and 35.6 GPa. Spectral regions corresponding to FSR-crosstalks are grayed out. Spectra associated with melting are highlighted in bold. (c) Brillouin shifts as a function of temperature at three representative pressures. Solid and liquid N_2 correspond to closed and open dots, respectively. Melting is indicated by the blue dashed line. (d) High pressure-high temperature melting curve of N_2. Open and closed symbols correspond to Brillouin data where the fluid peak is observed and not observed, respectively. Melting curves from literature are plotted for comparison.

A closeup look at the measured Stokes Brillouin peaks from N_2 along two heating

ramps are plotted in figures 8(a-b). Melting is clearly detected by the appearance of the fluid Brillouin peak (bold spectra). Figure 8(c) shows the Brillouin shifts in the solid and liquid samples as a function of temperature at three representative pressures [corresponding raw data are shown in figures 7(d) and 8(a-b)]. Melting is indicated by the vertical blue dashed line. Up to the highest pressure investigated (45.8 GPa), the frequency difference between the solid and fluid Brillouin peaks along the melting line remains close to 3 GHz.

Note that increasing temperature can lead to changes in the Brillouin shift or peak shape of solid N_2. These are likely due to the polycrystalline nature of the sample, leading to dispersion of sound velocities as function of the crystalline direction of the probed crystal(s) through elastic anisotropy. As temperature increases, especially near melting, fast re-crystallization occurs that can lead to a dispersion of data and jumps in the Brillouin shift evolution with temperature, a behavior commonly observed in high P-T Brillouin experiments on molecular crystals [9,46]. This may also be interpreted as structural phase transitions, with possible coexistence of molecular phases. For the whole data set, solid nitrogen is expected to be in the δ-phase. However, the presence of the ε phase due to axial temperature gradients cannot be ruled out. In any case, such Brillouin shift jumps are smaller than the one observed at melting.

The solid or fluid nature of the phase, extracted from Brillouin data, is plotted in the high pressure-high temperature phase diagram of nitrogen in figure 8(d). For both runs 1 and 2, the determined melting points are in good agreement with the consensual melting line obtained by various groups using a bulk microscopic detection of melting, either by Raman spectroscopy or by x-ray diffraction. Mukherjee and Boehler [42] reported a steeper melting line from the observation of movements in the laser speckle pattern, hence a surface effect so less reliable, as pointed out in ref. 47.

7. Conclusion

In summary, we have shown that the VIPA-based Brillouin spectrometer allows to perform Brillouin measurements more than ten times faster than when using the Tandem Fabry-Perot interferometer (TFP-1 model). This advantage comes at the cost of a fixed excitation wavelength, free spectral range and spectral resolution using the VIPA hyperfine instrument. Although an instrumental broadening of the Brillouin lines is observed with respect to the tandem interferometer, that does not affect the precision of the Brillouin shift determination nor the precision of the extracted sound velocity. High signal throughput is a major advantage for high-pressure experiments on tiny samples in the DAC, and more so for *in-situ* measurements under laser heating in which thermal stability and sample chemical integrity during acquisition are important issues. The implemented set-up shows excellent spatial filtering, which is also important for laser heating measurements in which radial temperature gradients in the sample can be large. Strict confocality ensures measuring a small and thus thermally homogeneous sample region.

The new method implemented in this work is offering new opportunities for high pressure science. Extending Brillouin measurement at higher pressures than before (that is, beyond 1 Mbar), in particular for the study of warm dense molecular systems under planetary interior conditions, will be of broad impact.

Acknowledgement(s)

The authors acknowledge Keevin Beneut for his help and the use of the spectroscopy platform of IMPMC, and the Agence Nationale de la Recherche for financial support under Grant n° ANR-21-CE30-0032-01 (LILI).

References

[1] Polian A. Brillouin scattering at high pressure: an overview. J Raman Spectrosc. 2003; 34:633–637.
[2] Zha CS, Mao HK, Hemley RJ. Elasticity of MgO and a primary pressure scale to 55 GPa. Proc Natl Acad Sci USA. 2000;97(25):13494–13499.
[3] Goncharov AF, Sinogeikin S, Crowhurst JC, et al. Cubic boron nitride as a primary calibrant for a high temperature pressure scale. High Press Res. 2007;27(4):409–417.
[4] Zhuravlev KK, Goncharov AF, Tkachev SN, et al. Vibrational, elastic, and structural properties of cubic silicon carbide under pressure up to 75 GPa: Implication for a primary pressure scale. J Appl Phys. 2013;113(11):113503.
[5] Polian A, Grimsditch M. Sound velocities and refractive index of densified a-SiO_2 to 25 GPa. Phys Rev B. 1993;47(21).
[6] Zha CS, Hemley RJ, Mao HK, et al. Acoustic velocities and refractive index of SiO_2 glass to 57. 5 GPa by Brillouin scattering. Phys Rev B. 1994;50(18).
[7] Polian A, Grimsditch M. New High-Pressure Phase of H_2O: Ice X. Phys Rev Lett. 1984; 52(15):4.
[8] Kimura T, Murakami M. Fluid-like elastic response of superionic NH_3 in Uranus and Neptune. Proc Natl Acad Sci USA. 2021;118(14):e2021810118.
[9] Ahart M, Karandikar A, Gramsch S, et al. High $P - T$ Brillouin scattering study of H_2O melting to 26 GPa. High Press Res. 2014;34(3):327–336.
[10] Giordano VM, Datchi F, Dewaele A. Melting curve and fluid equation of state of carbon dioxide at high pressure and high temperature. J Chem Phys. 2006;125(5):054504.
[11] Chen B, Gleason AE, Yan JY, et al. Elasticity, strength, and refractive index of argon at high pressures. Phys Rev B. 2010;81:144110.
[12] Ninet S, Weck G, Dewaele A, et al. Sound velocity and refractive index of pure N_2 fluid and of equimolar N_2–CO_2 fluid mixture up to 15 GPa. J Chem Phys. 2020;153(11):114503.
[13] Sandercock JR. Light Scattering in Solids III. Vol. 51. Berlin, Heidelberg: Springer Berlin Heidelberg; 1982. Chapter 6. Trends in brillouin scattering: Studies of opaque materials, supported films, and central modes; p. 173-206.
[14] Scarcelli G, Yun SH. Confocal Brillouin microscopy for three-dimensional mechanical imaging. Nat Photonics. 2008;2(1):39–43.
[15] Scarcelli G, Yun SH. Multistage VIPA etalons for high-extinction parallel Brillouin spectroscopy. Opt Express. 2011;19(11):10913.
[16] Fiore A, Zhang J, Shao P, et al. High-extinction virtually imaged phased array-based Brillouin spectroscopy of turbid biological media. Appl Phys Lett. 2016;108(20):203701.
[17] Zhang J, Scarcelli G. Mapping mechanical properties of biological materials via an add-on Brillouin module to confocal microscopes. Nat Protoc. 2021;16(2):1251–1275.
[18] Yan G, Bazir A, Margueritat J, et al. Evaluation of commercial virtually imaged phase array and Fabry-Pérot based Brillouin spectrometers for applications to biology. Biomed Opt Express. 2020;11(12):6933.
[19] Coker Z, Troyanova-Wood M, Traverso AJ, et al. Assessing performance of modern Brillouin spectrometers. Opt Express. 2018;26(3):2400.
[20] Benedetti LR, Loubeyre P. Temperature gradients, wavelength-dependent emissivity, and accuracy of high and very-high temperatures measured in the laser-heated diamond cell. High Press Res. 2004;24(4):423–445.

[21] Scarponi F, Mattana S, Corezzi S, et al. High-Performance Versatile Setup for Simultaneous Brillouin-Raman Microspectroscopy. Phys Rev X. 2017;7(3).
[22] Shirasaki M. Large angular dispersion by a virtually imaged phased array and its application to a wavelength demultiplexer. Opt Lett. 1996;21(5):366.
[23] Xiao S, Weiner AM, Lin C. A Dispersion Law for Virtually Imaged Phased-Array Spectral Dispersers Based on Paraxial Wave Theory. IEEE J Quantum Electron. 2004;40(4):420–426.
[24] Antonacci G, Lepert G, Paterson C, et al. Elastic suppression in Brillouin imaging by destructive interference. Appl Phys Lett. 2015;107(6):061102.
[25] Hollricher O. Confocal Raman Microscopy. (Springer Series in Optical Sciences; Vol. 158). Berlin, Heidelberg: Springer Berlin Heidelberg; 2011. Chapter 3. Raman Instrumentation for Confocal Raman Microscopy; p. 43-60.
[26] Abramson EH, Brown JM. Equation of state of water based on speeds of sound measured in the diamond-anvil cell. Geochim Cosmochim Acta. 2004;68(8):1827–1835.
[27] Polian A, Grimsditch M. Brillouin scattering from H_2O: Liquid, ice VI, and ice VII. Phys Rev B. 1983;27:6409–6412.
[28] Decremps F, Datchi F, Polian A. Hypersonic velocity measurement using Brillouin scattering technique. Application to water under high pressure and temperature. Ultrasonics. 2006;44:e1495–e1498.
[29] Baer BJ, Brown JM, Zaug JM, et al. Impulsive stimulated scattering in ice VI and ice VII. J Chem Phys. 1998;108(11):4540–4544.
[30] Sanchez-Valle C, Mantegazzi D, Bass JD, et al. Equation of state, refractive index and polarizability of compressed water to 7 GPa and 673 K. J Chem Phys. 2013;138(5):054505.
[31] Li F, Cui Q, He Z, et al. High pressure-temperature Brillouin study of liquid water: Evidence of the structural transition from low-density water to high-density water. J Chem Phys. 2005;123(17):174511.
[32] Meng Z, Yakovlev VV. Optimizing signal collection efficiency of the VIPA-based Brillouin spectrometer. J Innov Opt Health Sci. 2015;08(04):1550021.
[33] Turnbull R, Hanfland M, Binns J, et al. Unusually complex phase of dense nitrogen at extreme conditions. Nat Commun. 2018;9(1).
[34] Tomasino D, Jenei Z, Evans W, et al. Melting and phase transitions of nitrogen under high pressures and temperatures. J Chem Phys. 2014;140(24):244510.
[35] Gregoryanz E, Goncharov AF, Sanloup C, et al. High P-T transformations of nitrogen to 170 GPa. J Chem Phys. 2007;126(18):184505.
[36] Gregoryanz E, Goncharov AF, Hemley RJ, et al. Raman, infrared, and x-ray evidence for new phases of nitrogen at high pressures and temperatures. Phys Rev B. 2002;66(22).
[37] Goncharov AF, Crowhurst JC, Struzhkin VV, et al. Triple Point on the Melting Curve and Polymorphism of Nitrogen at High Pressure. Phys Rev Lett. 2008;101(9).
[38] Eremets MI, Gavriliuk AG, Trojan IA, et al. Single-bonded cubic form of nitrogen. Nat Mater. 2004;3(8):558–563.
[39] Laniel D, Geneste G, Weck G, et al. Hexagonal Layered Polymeric Nitrogen Phase Synthesized near 250 GPa. Phys Rev Lett. 2019;122:066001.
[40] Donadio D, Spanu L, Duchemin I, et al. *Ab initio* investigation of the melting line of nitrogen at high pressure. Phys Rev B. 2010;82(2).
[41] Yakub LN. Melting line of polymeric nitrogen. Low Temp Phys. 2013;39(5):427–429.
[42] Mukherjee GD, Boehler R. High-Pressure Melting Curve of Nitrogen and the Liquid-Liquid Phase Transition. Phys Rev Lett. 2007;99(22).
[43] Weck G, Datchi F, Garbarino G, et al. Melting Curve and Liquid Structure of Nitrogen Probed by X-ray Diffraction to 120 GPa. Phys Rev Lett. 2017;119(23).
[44] Shen G, Wang Y, Dewaele A, et al. Toward an international practical pressure scale: A proposal for an IPPS ruby gauge (IPPS-Ruby2020). High Press Res. 2020;40(3):299–314.
[45] Weck G, Queyroux JA, Ninet S, et al. Evidence and stability field of fcc superionic water ice using static compression. Phys Rev Lett. 2022;128:165701.
[46] Grimsditch M, Loubeyre P, Polian A. Brillouin scattering and three-body forces in argon

at high pressures. Phys Rev B. 1986;33:7192–7200.
[47] Gregoryanz E, Goncharov AF. Comment on "High-Pressure Melting Curve of Nitrogen and the Liquid-Liquid Phase Transition". Phys Rev Lett. 2009;102(4).